NANO · MICRO small
www.small-journal.com

Interlayer Engineering and Prelithiation: Empowering Si Anodes for Low-Pressure-Operating All-Solid-State Batteries

Seunggoo Jun, Gwanghyun Lee, Yong Bae Song, Haechannara Lim, Ki Heon Baeck, Eun Suh Lee, Ju Yeon Kim, Dae Woo Kim, Jong Hyeok Park, and Yoon Seok Jung**

Silicon (Si) anodes, free from the dendritic growth concerns found in lithium (Li) metal anodes, offer a promising alternative for high-energy all-solid-state batteries (ASSBs). However, most advancements in Si anodes have been achieved under impractical high operating pressures, which can mask detrimental electrochemo-mechanical issues. Herein, we effectively address the challenges related to the low-pressure operation of Si anodes in ASSBs by introducing an silver (Ag) interlayer between the solid electrolyte layer (Li_6PS_5Cl) and anode and prelithiating the anodes. The Si composite electrodes, consisting of Si/polyvinylidene fluoride/carbon nanotubes, are optimized for suitable mechanical properties and electrical connectivity. Although the impact of the Ag interlayer is insignificant at an exceedingly high operating pressure of 70 MPa, it substantially enhances the interfacial contacts under a practical low operating pressure of 15 MPa. Thus, Ag-coated Si anodes outperform bare Si anodes (discharge capacity: 2430 vs 1560 mA h g^{-1}). The robust interfacial contact is attributed to the deformable, adhesive properties and protective role of the in situ lithiated Ag interlayer, as evidenced by comprehensive ex situ analyses. Operando electrochemical pressiometry is used effectively to probe the strong interface for Ag-coated Si anodes. Furthermore, prelithiation through the thermal evaporation deposition of Li metal significantly improves the cycling performance.

1. Introduction

The growing demand for electrification in the automotive sector and energy storage systems has led to research on high-energy-density lithium–ion batteries (LIBs).[1,2] The concept of solidification of electrolytes using inorganic materials has garnered significant interest as a strategy for achieving substantial enhancements in energy density and safety.[3–5] Li metal and Si anodes are the most promising candidates for realizing this objective.[6–8]

Despite the ideal attributes of the lowest potential (−3.04 V vs standard hydrogen electrode) and the highest theoretical capacity (3860 mA h g^{-1}), the incorporation of Li metal anodes (LMAs) in all-solid-state batteries (ASSBs) has been hindered by several challenges.[3,6,9,10] These obstacles include the dendritic growth of Li metal[3,6,11-13,64,65] and restricted Li^+ diffusion in Li metal,[14] which lead to the formation of void spaces at the solid electrolyte (SE)–Li interfaces and high reactivity toward most SEs.[15–17] The latter leads to increased cell impedances, which adversely impact cell performance.[18] Recently, Lee et al. demonstrated the stable cycling of in situ generated LMAs for up to ≈1000 cycles in ASSBs with sulfide SEs and Ag-C anodes.[19] However, these results were obtained at an elevated temperature of 60 °C, which indicates the potential challenges related to kinetic constraints.

The absence of the limitations of LMAs in ASSBs could potentially provide advantageous conditions for Si anodes. Most early designs of Si anodes in ASSBs followed those of cathodes, consisting of composite electrodes containing Si, SEs, and conductive carbon additives with or without binders.[20–22] In LIBs, severe volume changes in Si (>300%) during charging and discharging can lead to cracks and fractures within both the electrode material and composite electrode, which causes a loss of electrical connectivity.[23–27] Furthermore, liquid electrolytes are decomposed on newly exposed Si surfaces continuously, leading to the formation of thick solid electrolyte interphase (SEI) layers, and severe performance degradation.[25,27–31] In ASSBs, high operating pressure helps maintain electrical and ionic connectivity within Si particles. However, the extreme volume changes in Si can cause cracks in the SE regions, which propagate laterally across the electrodes, and impeding the vertical transport of Li^+ ions.[32] Consequently, the operating pressure and SE deformability, although overlooked, significantly impact the performance of Si anodes in ASSBs.[20–22]

Another critical drawback of Si is its electrical insulating property.[33] Consequently, electrically wiring Si with nanostructured carbonaceous materials, such as carbon nanotubes (CNTs) and graphene, have been a common practice used for LIBs,[34–37] and this strategy has also been implemented in ASSBs.[38–40] A few exceptional strategies have been reported.[41–43] ASSBs with columnar structured Si deposited on the current collector

S. Jun, G. Lee, Y. B. Song, H. Lim, K. H. Baeck, E. S. Lee, J. Y. Kim, D. W. Kim, J. H. Park, Y. S. Jung
Department of Chemical and Biomolecular Engineering
Yonsei University
Seoul 03722, South Korea
E-mail: lutts@yonsei.ac.kr; yoonsjung@yonsei.ac.kr

The ORCID identification number(s) for the author(s) of this article can be found under https://doi.org/10.1002/smll.202309437

DOI: 10.1002/smll.202309437

achieved a promising cycling performance (capacity retention of 82% after 100 cycles, tested under a pressurized condition with a preset applied torque of 3.0 N m).[41] Tan et al. recently reported long-lasting Si ASSBs with micron-sized Si powders by eliminating SEs and carbon additives in the composite electrodes (the electrode composition was Si/polyvinylidene fluoride (PVDF) at a weight ratio of 99.9:0.1 and capacity retention of 80% after 500 cycles, tested at 50 MPa).[42] The underlying mechanism responsible for the outstanding performance was attributed to the mechanically sintering ability of lithiated Si and the absence of detrimental side reactions between sulfide SEs (Li_6PS_5Cl (LPSCl)) and carbon additives. However, in a recent comparative study, Si anodes with SEs, and carbon exhibited superior performance during initial cycles when compared with those without SEs and carbon.[44] As such, the effects of carbon materials on Si anodes in ASSBs remain unclear.[44,45]

It should be noted that the majority of the results obtained for Si ASSBs were achieved under exceedingly high operating pressures, such as 70 MPa. However, these pressures are not feasible for practical applications.[46–48] Increasing the operating pressure necessitates the use of larger compression devices, which translates into an increase in inactive components. This escalation directly undermines the system-level energy density. A significant challenge arises owing to the distinct difference in mechanical properties between the electrodes and SE layers in ASSBs, which make the interfaces susceptible to detachment.[47,49] This issue can be exacerbated in situations with no or low externally applied pressures, particularly when using breathing electrodes such as Si anodes.[50] A recent study reported a rapid capacity fading in Si electrodes utilizing $3LiBH_4$-LiI in Si||$LiNi_{0.80}Co_{0.15}Al_{0.05}O_2$ ASSB full-cells operating under a low-pressure of 10 MPa.[45] The capacity retention dropped to ≈30% after just 20 cycles, with an initial discharge capacity of 110 mA h g^{-1}. This performance is in stark contrast to the 74% retention over 100 cycles, with an initial discharge capacity of 152 mA h g^{-1}, achieved at the higher pressure of 70 MPa. We recently reported that 3D cross-linked binders can effectively mitigate interfacial failure in ASSBs operating under minimal or no pressures.[47]

In this study, we report a comprehensive design for Si ASSBs that incorporates a thin (≈40 nm) Ag interlayer at the interface between the Si electrodes and SE layer. In addition, the Si electrodes are tailored through integration with CNTs. The Ag interlayer, through alloying with Li during the charge–discharge cycling, retains deformable characteristics, and facilitates the maintenance of Li^+ transport across the interface, even with considerable dimensional changes in the Si anodes. This approach enables significant enhancements in the low-pressure operating performance of ASSBs at 15 MPa, as revealed by a complementary analysis using the peel-off test, cross-sectional scanning electron microscopy (SEM), ex situ X-ray photoelectron spectroscopy (XPS), time-of-flight secondary ion mass spectrometry (TOFSIMS), and operando electrochemical pressiometry measurements. Furthermore, we demonstrate additional advancements in the electrochemical performance of Si anodes at 15 MPa through prelithiation.

2. Results and Discussion

2.1. Si Anodes with Optimal Composition

To maintain consistency in terminology between full-cell and half-cell configurations, we define the lithiation process in half-cells as charging and the delithiation process as discharging. Si composite anodes with a composition of Si/PVDF at a weight ratio of 90:5 were tested using Si||Li-In half-cells at 30 °C initially under a conventional high operating pressure of 70 MPa. They exhibited high initial charge and discharge capacities of 3120 and 2630 mA h g^{-1}, respectively (Figure S1, Supporting Information). At the subsequent cycle with the pressure reduced to 15 MPa, these electrodes still demonstrated a high discharge capacity of 1980 mA h g^{-1}. This result can be attributed to the lithiated Si particles merging together to form a monolithic structure under the applied pressure. However, the capacity exhibited a significant decrease with each subsequent cycle. Moreover, when the Si anodes were initially subjected to a low operating pressure of 15 MPa, a negligible capacity was observed. This suggests that a pressure of 15 MPa may not be sufficient to achieve the mechanical integrity of Si particles and interfaces and/or ensure electrical connectivity within the electrodes considering the absence of carbon additives in their composition.

Si anodes with an insufficient fraction of binders exhibit poor mechanical properties, which can be detrimental to large-scale manufacturing processes. In this context, Si anodes prepared with varied electrode compositions, without or with CNTs, were subjected to 180° peel-off tests; and the results are displayed in **Figure 1a,b**. Corresponding videos of the universal testing machine experiment are provided in the Supporting Information (Videos S1–S3, Supporting Information). The peeling force of the commercial anode was ≈1 N cm^{-1} (**Figure 1a**). In contrast, the Si electrodes with Si/PVDF composition at 99:1 weight ratio were readily peeled off, with a peeling force of <0.1 N cm^{-1}. Furthermore, the Cu current collector was completely exposed owing to the delamination of the electrode layer, which is in stark contrast to the mere loss of surface on the stripped tape for the commercial electrode (Figure 1b). Incorporating 5 wt% binders increased the peeling force to 0.3–0.5 N cm^{-1}. With the addition of the 15 wt% binder, the peeling force reached 4 N cm^{-1}, which is sufficiently high when compared with commercial standards. To compensate for the reduced electronic conductivity of the electrodes containing excessive binders, the Si particles were uniformly coated with partially oxidized CNT through a simple slurry-cast process (Figure 1c; Figure S2, Supporting Information). These CNT coatings offer stable electron transport pathways and mechanical supports to the Si particles against harsh volume changes during cycling.[51] Consequently, the peeling force was significantly enhanced by incorporating CNTs, achieving a value of 5–6 N cm^{-1} (Figure 1a). Additionally, four-point probe measurements confirmed a substantial improvement in electrical resistance for Si electrodes incorporating CNTs. Specifically, Si electrodes with CNT (weight ratio of Si/CNT/PVDF = 70:15:15) exhibited an areal resistance that was 1/1000th of that measured for Si electrodes without CNTs (weight ratio of Si/PVDF = 95:5) (Figure S3, Supporting Information).

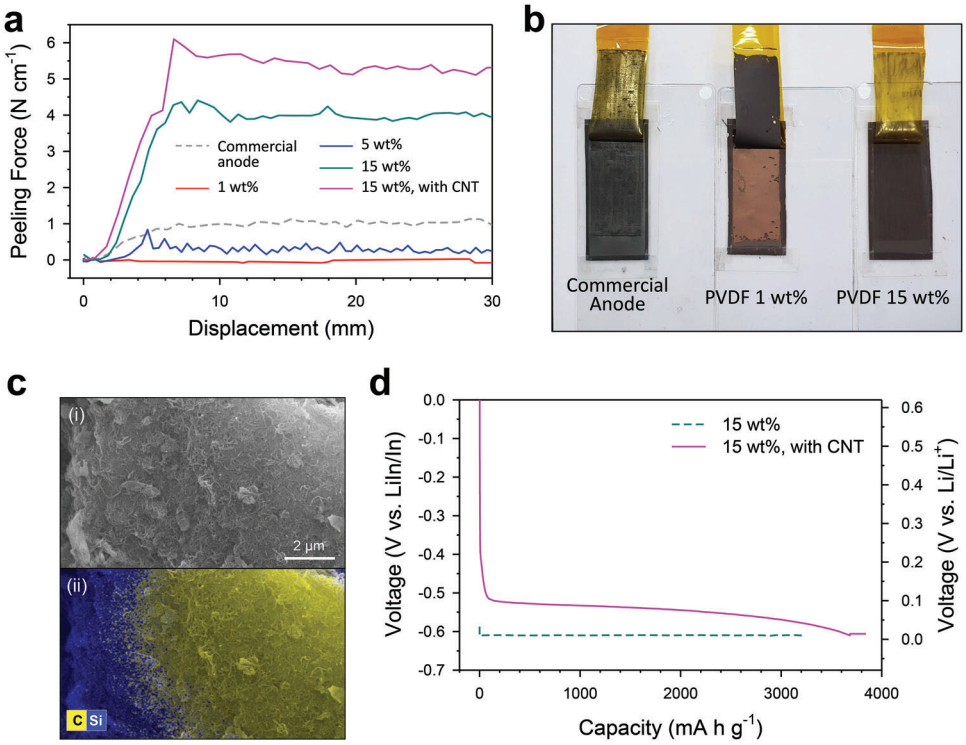

Figure 1. Si electrodes with varying polyvinylidene fluoride (PVDF) or carbon nanotube (CNT) content. a) Results obtained from the universal testing machine tests and b) corresponding photographs after peel-off tests. c) i) SEM image of Si electrodes prepared with 15 wt% PVDF and 15 wt% CNT, and ii) corresponding EDXS elemental map of C and Si. d) Initial charge voltage profiles in CCCV mode (constant current of 0.73 mA cm^{-2} and limiting current of 0.18 mA cm^{-2}) for Si electrodes prepared using 15 wt% PVDF without and with CNT.

The electrochemical performance of the Si electrodes with CNTs (weight ratio of Si/CNT/PVDF = 70:15:15) and without CNTs (weight ratio of Si/PVDF = 85:15) was assessed using Si||Li-In half-cells under a low operating pressure of 15 MPa at 30 °C and 0.2 C (0.74 mA cm^{-2}) in a constant-current constant-voltage (CCCV) mode (limiting current of 0.05C, Figure 1d). Upon initial charging, the voltage of the Si electrodes without CNT swiftly reached 0.01 V (vs Li/Li$^+$), after that the subsequent charging proceeded in the CV mode up to 3210 mA h g^{-1}, indicating a substantial overpotential. In stark contrast, the Si electrodes with CNTs displayed a lithiation plateau at ≈0.1 V (vs Li/Li$^+$) during the initial charging and delivered a high capacity of 3840 mA h g^{-1}. Reducing the fractions of the CNTs and binder (weight ratio of Si/CNT/PVDF = 90:5:5) led to degraded capacity retention (Figure S4, Supporting Information). Based on these results, it can be concluded that the Si electrodes with a composition of 70:15:15 (Si/CNT/PVDF) provide both electronic connectivity and mechanical support, which are essential for operating Si ASSBs under low applied pressure.

A comparative evaluation of Si electrodes under two different operating pressures (70 vs 15 MPa) was conducted using electrodes with an optimized composition (70:15:15); the results are displayed in **Figure 2**. Although the charge (lithiation) voltage profiles and capacities at 70 and 15 MPa were nearly identical, the discharge capacities decreased significantly from 2540 to 1560 mA h g^{-1} when the pressure was reduced from 70 to 15 MPa (Figure 2a). The corresponding cycling performance results are presented in Figure S5 (Supporting Information). A further reduction in the operating pressure down to 3 MPa led to a significant reduction in discharge capacity, dropping from 1560 to 510 mA h g^{-1} (Figure S6, Supporting Information). The cross-sectional SEM images of the electrodes before and after initial charging at 15 and 70 MPa are presented in Figure 2b. The results indicate a 240% increase in the electrode layer's thickness after charging. Significantly, the electrode layer was readily delaminated from the SE layer for charged (lithiated) at 15 MPa, which could be a contributing factor to the poor electrochemical performance (low discharge capacity). Si undergoes significant volume expansion upon charging, and side reaction products can form at the interfaces owing to the reaction between LPSCl and the lithiated phases including CNTs. These factors could exacerbate the interfacial contacts, further impacting the performance of the Si electrodes.

2.2. Deformable and Adhesive Ag Interlayer in Si||Li-In Half-Cells

To address the unstable interface issue, a design employing an adhesive mixed-conducting metallic Ag interlayer was devised, as depicted in **Figure 3**a. The lithiation reaction of Ag starts at ≈0.1 V (vs Li/Li$^+$), which is very close to the lithiation voltage of Si (Figure S7, Supporting Information). Consequently, an Ag interlayer forms lithiated alloys (Li$_x$Ag) during charging, functioning as an effective Li$^+$-conductive binding layer between the breathing Si electrode and SE layer. An Ag interlayer with a thickness

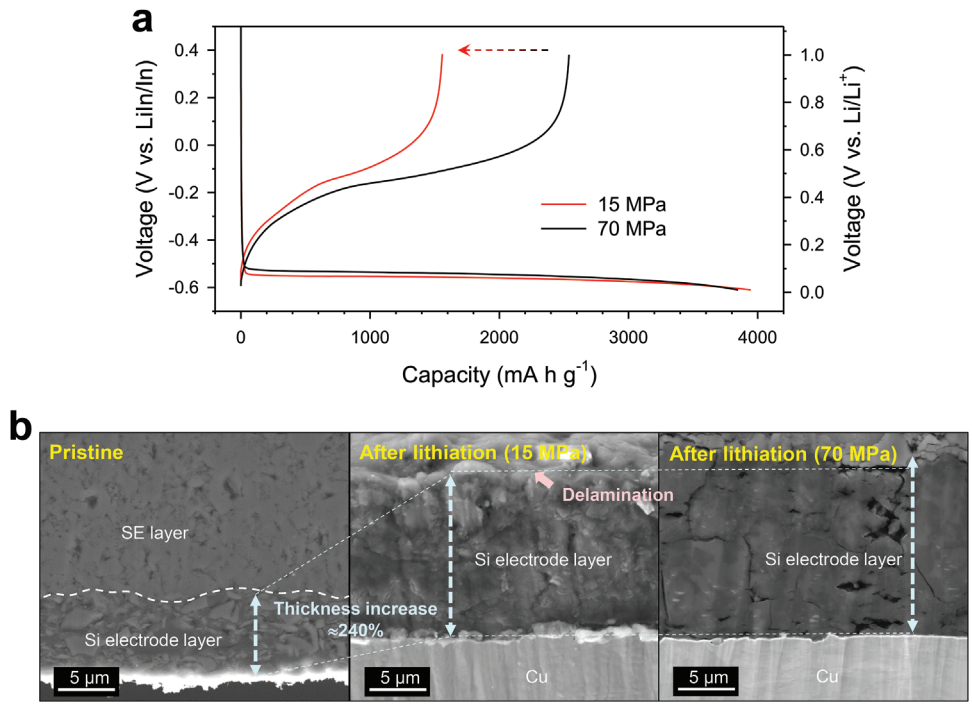

Figure 2. Results of Si electrodes in Si||Li-In all-solid-state half-cells operated under low-pressure. a) Initial charge–discharge voltage profiles at 30 °C of Si anodes at 15 and 70 MPa. b) Cross-sectional SEM images of Si electrodes before and after charging (lithiation) at 15 and 70 MPa. Note the delamination and thickness increase in the Si electrode after charging at 15 MPa.

of ≈40 nm was deposited on the Si electrodes (Si/PVDF/CNT weight ratio = 70:15:15) using direct current (DC) sputtering (Figure S8, Supporting Information). Bare and Ag-coated Si electrodes in the Si||Li-In half-cells were tested at 15 MPa, 30 °C, and 0.2 C. The initial charge–discharge voltage profiles and corresponding cycling performance with Coulombic efficiencies (CEs) are presented in Figure 3b,c, respectively. At the initial cycle, the charge capacities of the bare and Ag-coated Si electrodes indicated a marginal difference. However, the discharge capacity was substantially increased, approximately doubling from 1560 to 2430 mA h g^{-1} owing to the Ag interlayer coating. This result contrasts sharply with the insignificant difference in performance when a high operating pressure of 70 MPa was applied (Figure S9, Supporting Information). The superior performance of Ag-coated Si electrodes over bare electrodes at 15 MPa was also observed in the rate capability results (Figure S10, Supporting Information). Interestingly, both bare and Ag-coated Si electrodes exhibited similar poor cycling performances when tested using conventional liquid electrolytes (Figure S11, Supporting Information), highlighting the exceptional effect of the Ag interlayer in an ASSB system.

The drastic enhancement in performance by incorporating the Ag interlayer is attributed to its electrochemo-mechanical properties and protective role in preventing direct contact between the SE (LPSCl) and carbon (CNT). It should be noted that previous studies reported good adhesion properties exhibited by Ag.[52] As evidenced by the photographs displayed in Figure S12 (Supporting Information), lithiated Ag displayed significantly more deformable and sticky features when compared with pristine Ag, strongly supporting its positive role as the interlayer. The adhesion ability of the Ag interlayer was assessed by measuring the adhesive force between the Si anode and SE layer through a peel-off test. The cross-sectional SEM images exhibited in Figure S13 (Supporting Information) indicate that both bare and Ag-coated Si electrodes in their pristine states maintain firm contacts with the SE layer. Following the tests, the contacts between the SE and electrode layers persisted. However, it was observed that the Cu current collectors experienced delamination from the electrode layers during the testing process. Further, when the electrodes were discharged (delithiated) and subjected to a peel-off test, the electrode layer was readily delaminated for bare Si anodes, as depicted in the inset photograph in Figure 3b, and corresponding to a peeling force of 0 mN mm^{-1} (Figure 3d). In stark contrast, the Ag-coated Si electrodes exhibited a peeling force of 38.8 mN mm^{-1}.

Furthermore, given that the Si electrodes were charged down to 0 V (vs Li/Li^+), a voltage sufficient for the full lithiation of Ag and corresponding to Li_9Ag_4 alloy phase,[19] the mechanical properties of both Ag and Li_9Ag_4 pellets were examined using the nano-indentation method. Figure 3e presents a representative force–displacement curve at room temperature, and the corresponding values of the Young's modulus and hardness are plotted in Figure 3f. At the peak load of 500 μN, Li_9Ag_4 exhibited a displacement value of 572 nm, and that is larger than that of Ag (335 nm) (Figure 3e), signifying increased deformability. Following lithiation, the values of both the Young's modulus and hardness also decreased significantly from 34.1 to 4.3 GPa and from 0.81 to 0.38 GPa, respectively. This confirms the substantially improved deformability of Li_9Ag_4 when compared with Ag. It should be noted that the values of Young's modulus and

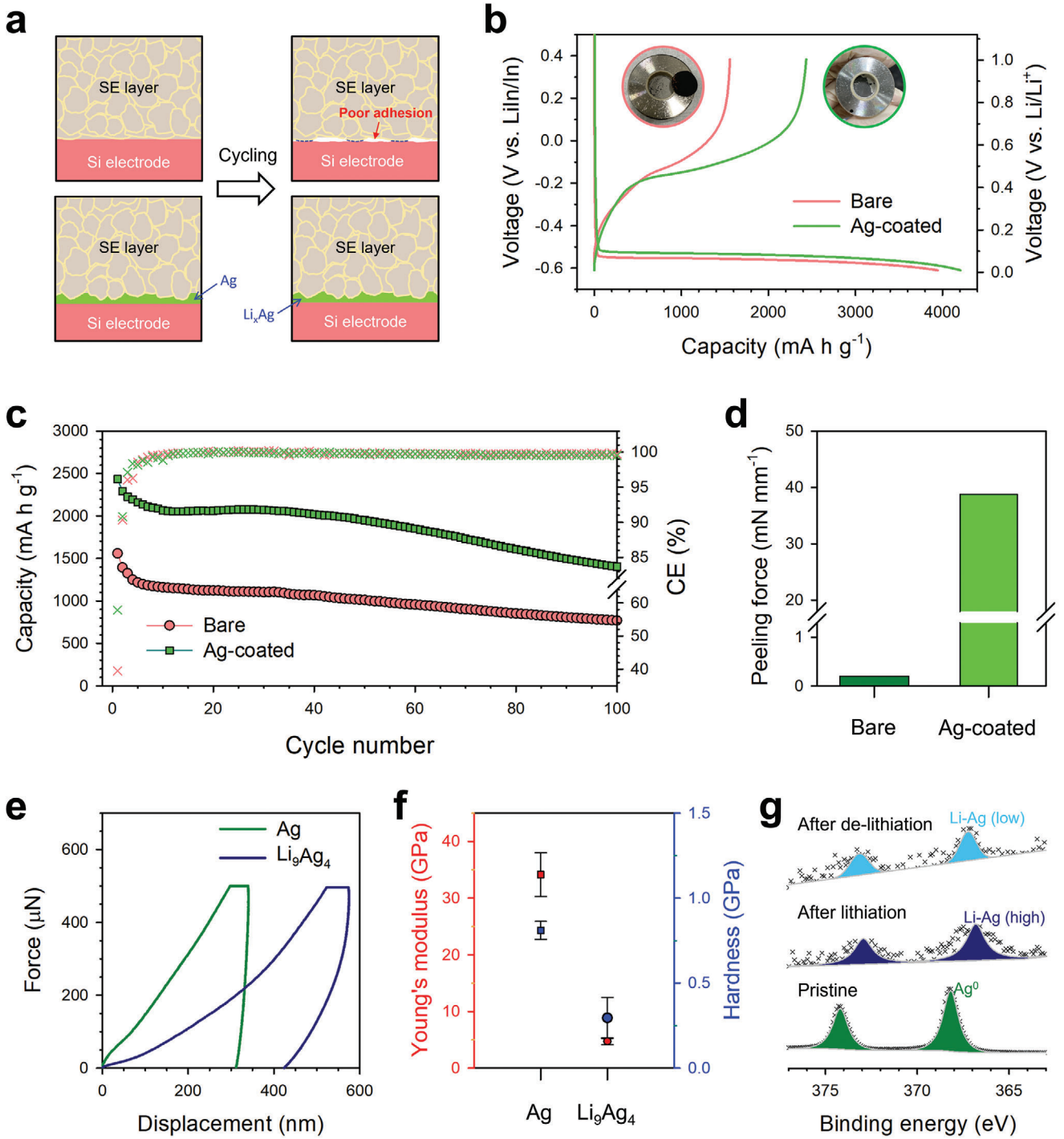

Figure 3. Results of Ag-coated Si electrodes. a) Schematic illustrating Si–SE interfaces for bare and Ag-coated Si electrodes upon cycling. b) Initial charge–discharge voltage profiles of bare and Ag-coated Si electrodes in Si||Li-In all-solid-state half-cells at 15 MPa, 30 °C, and 0.2 C, and c) corresponding cycle performances with CEs. The inset of b) presents the photographs of cells after the initial discharging, highlighting the absence of delamination for Ag-coated Si anodes in contrast to the delamination observed in bare Si anodes. d) Results of peel-off test for bare and Ag-coated Si electrodes after discharging (de-lithiation). e) Quasistatic nanoindentation curves of pristine and lithiated Ag (Li_9Ag_4), and f) corresponding values of Young's modulus and hardness. g) XPS Ag 3*d* spectra of Ag-coated Si electrodes before cycling, after charging (lithiation) and discharging (delithiation).

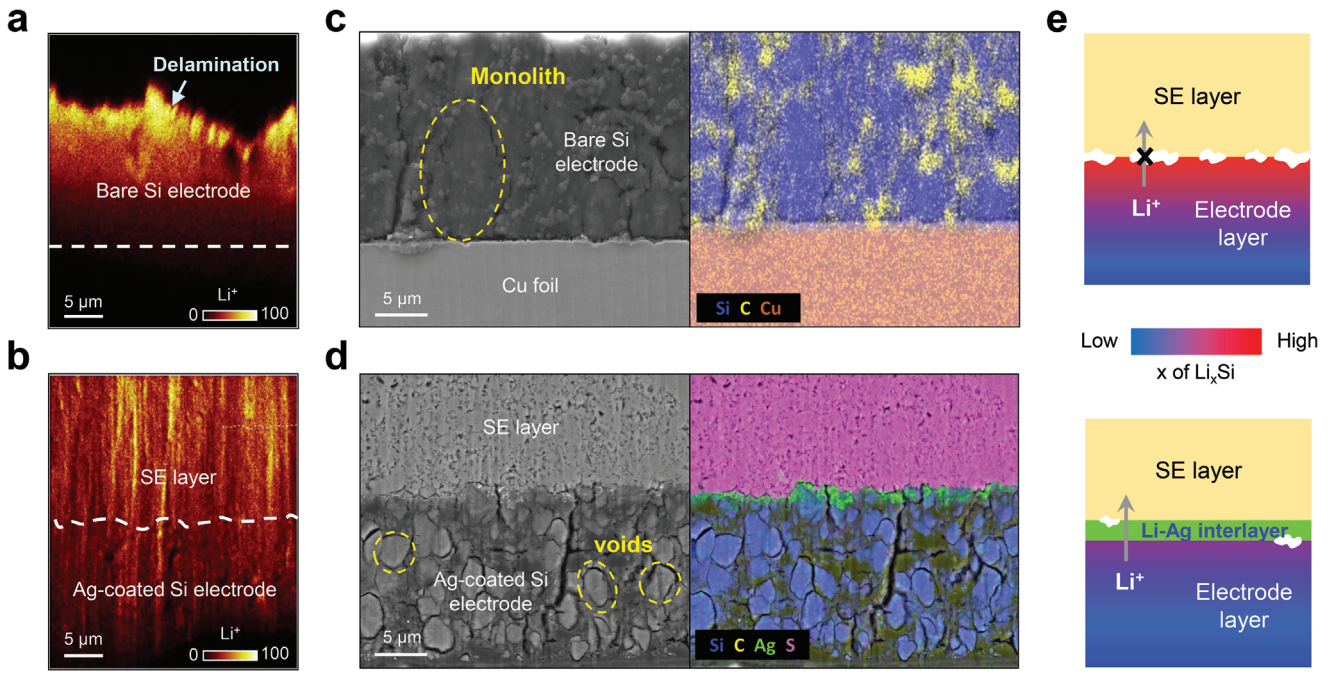

Figure 4. TOFSIMS results of SE–Si interfaces for bare and Ag-coated Si electrodes after discharging (delithiation). Cross-sectional TOFSIMS maps of Li^+ ions for a) bare and b) Ag-coated Si electrodes. Cross-sectional SEM images and corresponding EDXS elemental maps of c) bare and d) Ag-coated Si electrodes. e) Schematic depicting the variations in state of charge (SOC) across the depth of Si electrodes with and without Ag interlayer.

hardness for Li_9Ag_4 were considerably lower when compared with lithiated Si (8.1 and 0.9 GPa, respectively; Figure S14, Supporting Information).[53]

The ex situ XPS Ag 3*d* spectra of pristine, charged, and discharged Ag-coated Si electrodes are depicted in Figure 3g. The main peak of the pristine sample at 368.3 eV was shifted negatively to 366.9 eV after charging (lithiation), signifying the lithiation of Ag. Following discharging (delithiation), the peak shifted slightly positively to 367.2 eV,[54] still indicating lithiated phases. These results suggest that the advantageous properties of lithiated Ag remain effective during cell cycling. In addition, an Ag interlayer can effectively prevent deleterious side reactions between LPSCl and CNT.[42] The ex situ XPS analysis of Ag-coated Si electrodes after one cycle revealed a substantially reduced evolution of Li_2S compared to the bare electrodes (Figure S15, Supporting Information). Li_2S is known as reductive decomposition byproduct of LPSCl,[66] likely resulting primarily from side reactions with carbon (CNT). The mitigated side reaction observed in the Ag-coated Si electrodes underscores the effectiveness of the Ag interlayer in enhancing interfacial stability.

In conclusion, the highly deformable and adhesive properties of the lithiated Ag interlayer, combined with its protective role, enable it to accommodate severe dimensional changes, and stresses in Si electrodes while maintaining intimate interfacial contacts. This significantly enhances the low-pressure operation performance of ASSB cells.

A comprehensive analysis of the underlying electrochemical mechanism was conducted through TOFSIMS measurements; the results are presented in **Figures 4** and S16 (Supporting Information). Figure 4a,b display the Li^+ maps of the cross-sectioned SE–electrode interfaces for bare Si and Ag-coated Si electrodes after the initial discharging (delithiation). For bare Si electrodes, Li^+ is concentrated in the delaminated surface regions, suggesting that the Li^+ transport pathways might have been hindered or disconnected at the interface during cycling (Figure 4a), which is supported by the peel-off test results (Figure 3d). In contrast, the Li^+ concentration is evenly distributed across the interfaces for Ag-coated Si electrodes, indicating that the Li^+ transport pathways across the interfaces are effectively preserved during cycling (Figure 4b; Figure S16, Supporting Information). The corresponding cross-sectional SEM images and energy dispersive X-ray spectroscopy (EDXS) elemental maps are displayed in Figure 4c,d. The bare Si electrodes after initial discharging exhibit a monolithic characteristic, indicating a high state of charge (SOC), or low depth of discharge (DOD). In contrast, void spaces are observed in the discharged Ag-coated Si electrodes, indicating a higher DOD, which should result from the facile Li^+ extraction through the well-maintained SE–electrode interfaces through the lithiated Ag interlayer, as illustrated in Figure 4e.

2.3. Si||$LiNi_{0.70}Co_{0.15}Mn_{0.15}O_2$ Full-Cells with Ag Interlayer Under Low-Pressure

Si||$LiNi_{0.70}Co_{0.15}Mn_{0.15}O_2$ (NCM) all-solid-state full-cells were assembled using bare or Ag-coated Si anodes and tested in the voltage range of 2.50–4.29 V at 30 °C, 0.2C (0.44 mA cm^{-2}), and 15 MPa. The corresponding results are presented in **Figure 5**. The electrochemical performance of NCM in NCM||Li-In half-cells is depicted in Figure S17 (Supporting Information). The mass loadings of NCM and Si were 11 and 0.94–1.05 mg cm^{-2}, respectively. Full-cell balance was designed to utilize ≈65% of the full

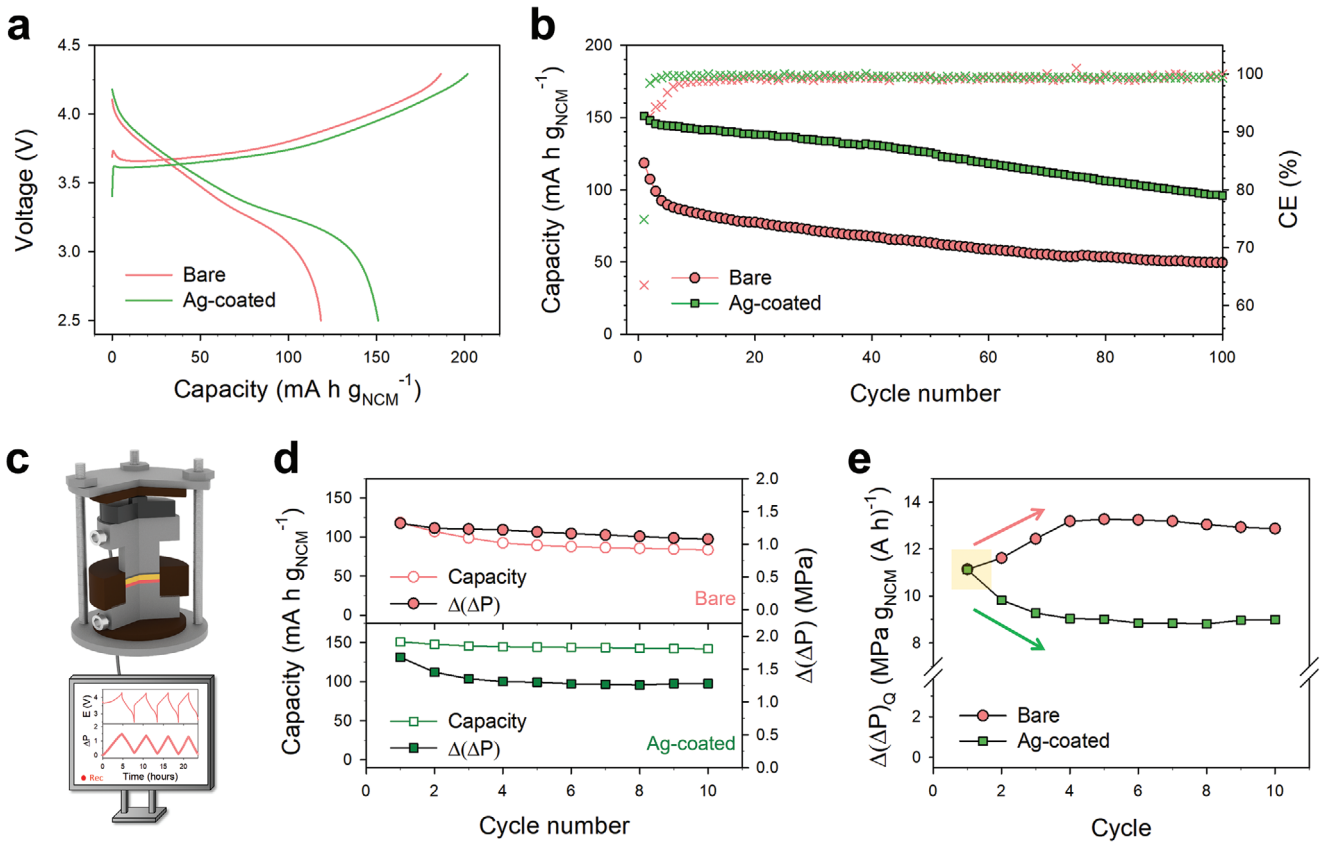

Figure 5. Electrochemical performance results at 15 MPa and 30 °C for NCM||Si all-solid-state full-cells employing bare or Ag-coated Si anodes. a) Initial charge–discharge voltage profiles at 0.2 C and b) corresponding cycling performances with CEs. c) Schematic of operando electrochemical pressiometry setup with representative voltage profiles and corresponding pressure change profiles (ΔP). d) Discharge capacity as a function of cycle number with corresponding pressure change differences ($\Delta(\Delta P)$). e) Capacity-normalized pressure change difference ($\Delta(\Delta P)_Q$) as a function of cycle number. f) Schematic of interfacial evolution affecting the pressure change behavior.

charge capacity of the Si anodes, based on the results obtained from NCM||Li-In, and Si||Li-In half-cells. Owing to the low initial CEs (ICEs) of Si anodes under low-pressure, the discharging of full-cells ended upon the termination of the Si anodes (Figure S18, Supporting Information).

The initial charge–discharge voltage profiles of the Si||NCM full-cells, along with their corresponding cycling performance, are displayed in Figure 5a,b, respectively. The charge capacities indicated only a slight difference between using Ag-coated and bare Si electrodes: 201 versus 186 mA h g_{NCM}^{-1}, respectively. However, the discharge capacity for Ag-coated Si electrodes was significantly larger than that for bare Si electrodes (151 vs 119 mA h g_{NCM}^{-1}). These results align well with half-cell data (Figure 3b,c), as the discharge capacity is determined by the Si anode. Full-cells employing bare and Ag-coated Si electrodes displayed capacity retentions of 42% and 64% after 100 cycles, respectively (Figure 5b). It should be noted that when tested under a high-pressure of 70 MPa, both full-cells with bare, and Ag-coated Si anodes exhibited comparable capacities (Figure S19, Supporting Information). This outcome emphasizes that under conventional high-pressure operating conditions, certain practically significant factors might be overlooked.

In addition, the electrochemo-mechanical evolution in Si||NCM full-cells was investigated through operando monitoring of pressure changes during the charging and discharging processes (Figure 5c). Representative charge–discharge voltage and corresponding pressure-varying profiles are depicted in Figure S20 (Supporting Information). Owing to the larger volume change in Si upon Li insertion/extraction when compared with NCM, the overall pressure changes follow those of Si anodes.[50] Figure 5d displays the discharge capacities and pressure change differences (denoted by $\Delta(\Delta P)$) of Si||NCM full-cells as a function of cycle number for bare and Ag-coated Si anodes. Intriguingly, the cells with bare and Ag-coated Si anodes demonstrated distinct characteristics in terms of changes in capacity and $\Delta(\Delta P)$. During the initial four cycles, the cells with bare Si anodes exhibited a faster decrease in capacity relative to $\Delta(\Delta P)$, whereas the cells with Ag-coated Si anodes displayed the opposite trend. This remarkable behavior becomes more apparent when plotting pressure change differences normalized with respect to capacity at each cycle ($\Delta(\Delta P)_Q$) (see Figure 5e).[55] $\Delta(\Delta P)_Q$ increased upon cycling for bare Si anodes, whereas it decreased for Ag-coated Si anodes. As indicated by the peel-off test and TOFSIMS results presented in Figures 3d and 4, respectively, cells without the Ag interlayer exhibited degraded SE–electrode interfaces upon cycling. In contrast, those with the Ag interlayer indicated robust interfaces, as illustrated in Figure 3a. As interfacial degradation progresses, the interfacial

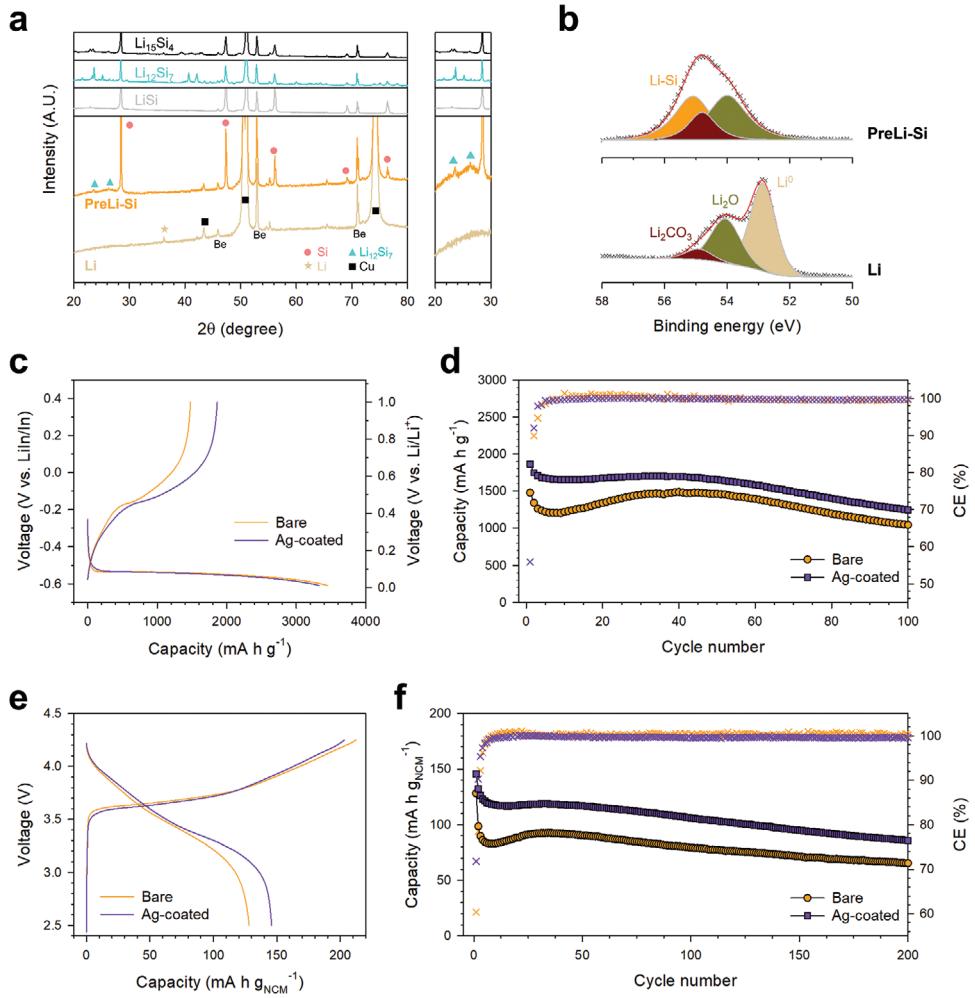

Figure 6. Results of prelithiated Si electrodes in ASSBs under low operating pressure of 15 MPa. a) Ex situ XRD patterns and b) Li 1s XPS spectra of thermally deposited Li metal on Cu foil and prelithiated Si electrodes. c) Initial charge–discharge voltage profiles at 0.2 C and 30 °C for prelithiated Si electrodes without or with Ag coating in Si||Li-In half-cells at 15 MPa, and d) corresponding cycling performances with CEs. e) Initial charge–discharge voltage profiles at 0.2 C and 30 °C for prelithiated Si electrodes without or with Ag coating in NCM||Si full-cells at 15 MPa, and f) corresponding cycling performances with CEs.

contact area decreases significantly along with the evolution of void spaces, suggesting that the internal pressure caused by Si volume expansion should increase, as illustrated in Figure S21 (Supporting Information).[55] Therefore, the increase in $\Delta(\Delta P)_Q$ upon cycling for bare Si anodes aligns well with the deterioration of interfacial contacts. In contrast, the decrease in $\Delta(\Delta P)_Q$ upon cycling for Ag-coated Si anodes provides strong evidence for the maintenance of robust interfacial contacts.

2.4. Prelithiation of Si Anodes

Despite the significant capacity improvement achieved through the Ag interlayer, addressing the issue of gradual capacity fading still remains a challenge. Prelithiation of Si anodes could be an effective solution to tackle this issue. First, it provides an excess Li reservoir to compensate for the ongoing loss of Li during each cycle.[56,57] Second, prelithiation ensures that Si anodes maintain high SOC, in which their deformable properties are preserved, and thereby enhancing low-pressure operability.

Prelithiation of bare or Ag-coated Si anodes was carried out by depositing Li metal on the electrodes using a thermal evaporator.[58] Even after Li deposition, the surface of the Si electrodes looked matte, indicating the facile alloying reaction between as-deposited Li and Si (Figure S22, Supporting Information).[59] The thickness of the deposited Li metal was ≈2.5 µm, which corresponds to an SOC level of x in Li_xSi: 1.1 for a composition between LiSi and $Li_{12}Si_7$. **Figure 6a** displays the XRD patterns of the prelithiated bare Si electrode (denoted as "PreLi-Si," whereas prelithiated Ag-coated Si is denoted as "PreLi-Ag-Si") and the electrode where Li metal was deposited on Cu foil. The PreLi-Si sample exhibited no Li metal signals, with the weak peaks corresponding to $Li_{12}Si_7$ (represented by sky blue triangles). The surface XPS results for PreLi-Si and Li metal, as seen in Figure 6b, also confirm the formation of the lithiated Si alloy phase at 55 eV, with surface impurities such as Li_2O and

Li_2CO_3.[60] Consistently, XRD measurements for PreLi-Ag-Si revealed the presence of the lithiated Si phase ($Li_{12}Si_7$), alongside the emergence of a lithiated Ag phase (Li_9Ag_4), and the disappearance of Ag (Figure S23, Supporting Information).

Figure 6c,d present the initial charge–discharge voltage profiles and corresponding cycling performances with CEs for PreLi-Si and PreLi-Ag-Siin Si||Li-In half-cells at 30, 0.2 °C, and 15 MPa. When compared with the data without prelithiation displayed in Figure 3b,c, prelithiated Si electrodes exhibited no improvements in capacity. The initial discharge capacities for bare and Ag-coated Si anodes were 1560 and 2430 mA h g^{-1}, respectively, whereas those after prelithiation were 1480 and 1860 mA h g^{-1}. Importantly, the capacity enhancement provided by the Ag coating remained effective for the prelithiated electrodes. Furthermore, the capacity retention for both bare and Ag-coated Si anodes was substantially improved through prelithiation: After 100 cycles, the capacity retention for bare and Ag-coated Si anodes increased to 70% and 67%, respectively, compared to 49% and 58% without prelithiation. Finally, PreLi-Si||NCM and PreLi-Ag-Si||NCM full-cells were evaluated at 30 °C, 0.2 C, and 15 MPa (Figure 6d,e). The initial discharge capacity of PreLi-Ag-Si was considerably higher than that of Pre-Li-Si (146 vs 128 mA h $g_{NCM}{}^{-1}$). Remarkably, PreLi-Ag-Si demonstrated a remarkable capacity retention of 73% after 100 cycles (59% after 200 cycles), which presents a significant improvement when compared with the cells without prelithiation (42% after 100 cycles, Figure 5b).

3. Conclusion

In summary, the challenges associated with the low-pressure operation of Si anodes in ASSBs were effectively addressed by implementing the design strategy of incorporating an Ag interlayer between the SE layer and anode as well as prelithiation of the anodes. Si electrodes with both suitable mechanical properties and electrical connectivity require substantial amounts of binder PVDF and CNT (e.g., 15 wt% of each). Implementing an Ag interlayer significantly improves interfacial contacts, particularly when the Si anodes were discharged (delithiated). Thus, Ag-coated Si anodes in both Si||Li-In half-cells and Si||NCM full-cells outperformed bare Si anodes under the practically relevant low operating pressure of 15 MPa in terms of discharge capacity (for example, the initial discharge capacities were 2430 and 1560 mA h g^{-1}, respectively). The Ag interlayer can act as an effective barrier against the detrimental side reactions between the SE (LPSCl) and carbon (CNT). Notably, the robust interfacial contact observed with Ag-coated Si anodes was attributed to the deformable and adhesive properties of the in situ lithiated Ag interlayer, as comprehensively supported by ex situ XPS, nano-indentation, peel-off test, cross-sectional SEM, and ex situ TOF-SIMS results. Moreover, the robust interface for Ag-coated Si anodes, in contrast to the interfacial degradation for bare Si anodes, could be successfully probed by a capacity-normalized pressure change difference $\Delta(\Delta P)_Q$ using operando electrochemical pressiometry. Finally, it was successfully demonstrated that prelithiation through thermal evaporation deposition of Li metal on Si anodes could significantly improve the cycling performance of Si anodes under the low-pressure operating condition of 15 MPa (e.g., 73% capacity retention after 100 cycles with an initial discharge capacity of 146 mA h $g_{NCM}{}^{-1}$ for PreLi-Ag-Si||NCM full-cells versus 42% capacity retention with an initial capacity of 118 mA h $g_{NCM}{}^{-1}$ for Si||NCM full-cells). We believe that our findings and design strategies offer essential guidelines for the development of high-energy ASSBs with a considerable impact on practical applications.

4. Experimental Section

Preparation of Materials: Si powders of size 1–5 µm (99.9% metal basis) were purchased from Alfa Aesar. PVDF binders obtained from Arkema (Kynar, HSV-900) were used. Oxidized CNTs dispersed in water were prepared using a modified Hummer's method.[51] Multiwalled CNTs (MWCNTs, JenoTube 20A, and diameters of 15–25 nm) were treated with sulfuric acid (H_2SO_4), followed by the gradual addition of potassium permanganate ($KMnO_4$). After 1 h, deionized water and hydrogen peroxide (H_2O_2) were introduced to terminate the reaction. The CNT dispersion was then dried in a vacuum oven, and oxidized CNT powders were obtained. Argyrodite LPSCl (Li_6PS_5Cl) powders, obtained from CIS Co. Ltd, were used, exhibiting an Li^+ conductivity of 2.8 mS cm^{-1} at 30 °C, and that was determined using the alternating current (AC) method with Ti|SE|Ti symmetric cells. The NCM powders were coated with 1.4 wt% $LiNbO_3$ using a wet-chemical method employing lithium ethoxide (99.95%, Sigma–Aldrich), and niobium ethoxide (99.95%, Sigma–Aldrich), as described in a previous work.[61,62] Conductive carbon additives (Super C65) were obtained from TIMCAL Ltd.

Fabrication of Electrodes: Si composite slurries were prepared by mixing Si powers, PVDF, and CNT at a target ratio using N-methyl-2-pyrrolidine (NMP, Sigma–Aldrich) as a solvent. The slurries were then cast onto a Cu current collector and dried in a vacuum oven at 80 °C. Ag coatings were applied on the Si anodes using a sputter coater (108 auto, Cressington Scientific Instruments Ltd) at 30 mA for 80 s, resulting in a thickness of 40 nm. For the prelithiation of Si electrodes, Li metal was deposited using a thermal evaporator (WOOSUNG HI-VAC Co.) housed within an Ar-filled glove box. A piece of solid Li was placed inside a Ta boat within the evaporator. Following evacuation to a pressure of $<10^{-6}$ Torr, Li was evaporated from the heated boat at a deposition rate of 2 nm s^{-1} for 1250 s, and a 2.5 µm-thick layer of Li was deposited onto the Si electrodes. To prepare $Li_{0.5}$In-SE counter electrodes, the $Li_{0.5}$In powders were initially produced by mixing Li (FMC Lithium Corp.) and In (Aldrich, 99%) powders. Subsequently, these $Li_{0.5}$In powders were blended with SE (LPSCl) powders, leading to the formation of $Li_{0.5}$In-SE counter electrodes.[13] The galvanostatic test results of the $Li_{0.5}$In-SE counter electrodes for obtaining overpotentials are described in the Supporting Information (Figure S24, Supporting Information). For the preparation of composite cathodes, NCM, LPSCl, and super C65 were mixed in a weight ratio of 70:30:3 using a mortar and pestle.

Material Characterization: The adhesion forces of electrodes were measured using a 180° peel-off test with a Universal Testing Machine (Lloyd Instruments) at a peel speed of 200 mm min^{-1}. Tapes were uniformly attached to the electrodes using a 500 g metal rod. The average peeling force values were calculated after the first peak, up to a displacement of 30 mm. For the nano-indentation tests, Ag and Li_9Ag_4 pellets (of diameter 6 mm) were prepared using uniaxial pressing powders at 370 MPa. The equations for obtaining the modulus are described in the Supporting Information. A maximum force of 500 µN was applied as the controlled indentation load using a PI-85 instrument (Bruker Corp.). For the XRD measurements, the samples were hermetically sealed with a Be window. They were mounted on a Rigaku MiniFlex 600 diffractometer and subjected to measurements using Cu K_α radiation (1.5406 Å) in a 2θ scanning range of 10°–80° with a step size of 0.02° at 40 kV and 15 mA. Cross-sectional field-emission SEM images were obtained by cold-polishing the samples at 6.0 kV for 6 h, followed by 1.5 kV milling for 1 h with an Ar ion beam at 30 °C (JEOL, IB19510CP). The SEM images and corresponding EDXS elemental maps were acquired using AURIGA (CarlZeiss). The sample specimens were stored and transported using an airtight system shuttle to prevent exposure to ambient air. Ex situ XPS measurements

were performed using a monochromatic Al K_α source (1486.6 eV) at 12 kV and 6 mA using K-Alpha+ (Thermo Fisher Scientific). The samples were mounted on a sample holder in an Ar-filled glove box and transferred to the XPS equipment without exposure to ambient air. TOFSIMS analyses were conducted on a TOF SIMS 5 (ION-TOF GmbH, Heisenbergstrabe, and Munster). A 30 keV pulsed Bi^{3+} ion source was employed for analysis and sputtering. The TOFSIMS imaging areas were $50 \times 50\ \mu m^2$ for the cross-sectioned Si electrode samples. The base pressure of the analysis chamber was maintained at $<5.0 \times 10^{-10}$ Pa during all the measurements.

Electrochemical Characterization: All-solid-state cells (diameter of 13 mm), consisting of Ti rods as the current collectors and a polyaryletheretherketone mold, were used. To fabricate all-solid-state Si half-cells, an LPSCl layer was formed by pelletizing 150 mg of LPSCl by pressing at 70 MPa for 3 min. Subsequently, a working electrode (bare or Ag-coated Si electrode) with a diameter of 12.7 mm was attached to one side of the SE layer (LPSCl), whereas an $Li_{0.5}$In-LPSCl counter electrode was placed on the other side. The entire assembly was pressed at a pressure of 370 MPa. Si half-cells were cycled at 0.2 C and 30 °C in the voltage range of 0.01–1.00 V versus Li/Li^+ under an external applied pressure of 15 or 70 MPa. To fabricate all-solid-state full-cells, the NCM cathodes were placed on one side of the SE layer (150 mg) prepared at 70 MPa. Either a bare or an Ag-coated Si electrode was positioned on the other side of the SE layer, and the entire assembly was pressed at 370 MPa. All-solid-state full-cells were cycled at 0.2 C and 30 °C. For operando electrochemical pressiometry measurements, a pressure sensor with a resolution of 0.1 kg (load cell, BONGSHIN) was placed in the pressurized cell, as described in the previous work.[63] The changes in pressure during charging and discharging were monitored using in-house software. All the processes for fabricating the electrodes were conducted in an Ar-filled dry glove box.

Supporting Information

Supporting Information is available from the Wiley Online Library or from the author.

Acknowledgements

S.J. and G. Lee contributed equally to this work. This work was supported by the Technology Development Program to Solve Climate Changes through the National Research Foundation of Korea (NRF) funded by the Ministry of Science, ICT & Future Planning (2022M3J1A1085397) and by the technology innovation program (20012216) funded by the Ministry of Trade, Industry & Energy (MOTIE, Korea).

Conflict of Interest

The authors declare no conflict of interest.

Data Availability Statement

The data that support the findings of this study are available from the corresponding author upon reasonable request.

Keywords

interfaces, low pressure, pre-lithiation, silicon anodes, solid-state batteries

Received: October 20, 2023
Revised: November 23, 2023
Published online:

[1] J. W. Choi, D. Aurbach, *ACS Appl. Energy Mater.* **2016**, *1*, 16013.
[2] H. Li, *Joule* **2019**, *3*, 911.
[3] J. Janek, W. G. Zeier, *Nat. Energy* **2016**, *1*, 16141.
[4] A. Manthiram, X. Yu, S. Wang, *Nat. Rev. Mater.* **2017**, *2*, 16103.
[5] H. Kwak, J.-S. Kim, D. Han, J. S. Kim, J. Park, G. Kwon, S.-M. Bak, U. Heo, C. Park, H.-W. Lee, K.-W. Nam, D.-H. Seo, Y. S. Jung, *Nat. Commun.* **2023**, *14*, 2459.
[6] S. Xia, X. Wu, Z. Zhang, Y. Cui, W. Liu, *Chem* **2019**, *5*, 753.
[7] H. Huo, J. Janek, *ACS Energy Lett.* **2022**, *7*, 4005.
[8] J. A. Lewis, K. A. Cavallaro, Y. Liu, M. T. Mcdowell, *Joule* **2022**, *6*, 1418.
[9] K. B. Hatzell, X. C. Chen, C. L. Cobb, N. P. Dasgupta, M. B. Dixit, L. E. Marbella, M. T. Mcdowell, P. P. Mukherjee, A. Verma, V. Viswanathan, A. S. Westover, W. G. Zeier, *ACS Energy Lett.* **2020**, *5*, 922.
[10] K. Yoon, S. Lee, K. Oh, K. Kang, *Adv. Mater.* **2022**, *34*, 2104666.
[11] F. Han, A. S. Westover, J. Yue, X. Fan, F. Wang, M. Chi, D. N. Leonard, N. J. Dudney, H. Wang, C. Wang, *Nat. Energy* **2019**, *4*, 187.
[12] J. Kasemchainan, S. Zekoll, D. Spencer Jolly, Z. Ning, G. O. Hartley, J. Marrow, P. G. Bruce, *Nat. Mater.* **2019**, *18*, 1105.
[13] Y. J. Nam, K. H. Park, D. Y. Oh, W. H. An, Y. S. Jung, *J. Mater. Chem.* **2018**, *6*, 14867.
[14] T. Krauskopf, B. Mogwitz, C. Rosenbach, W. G. Zeier, J. Janek, *Adv. Energy Mater.* **2019**, *9*, 1902568.
[15] J. A. Lewis, F. J. Q. Cortes, Y. Liu, J. C. Miers, A. Verma, B. S. Vishnugopi, J. Tippens, D. Prakash, T. S. Marchese, S. Y. Han, C. Lee, P. P. Shetty, H.-W. Lee, P. Shevchenko, F. De Carlo, C. Saldana, P. P. Mukherjee, M. T. Mcdowell, *Nat. Mater.* **2021**, *20*, 503.
[16] Z. Ning, D. S. Jolly, G. Li, R. De Meyere, S. D. Pu, Y. Chen, J. Kasemchainan, J. Ihli, C. Gong, B. Liu, D. L. R. Melvin, A. Bonnin, O. Magdysyuk, P. Adamson, G. O. Hartley, C. W. Monroe, T. J. Marrow, P. G. Bruce, *Nat. Mater.* **2021**, *20*, 1121.
[17] M. Yang, Y. Mo, *Angew. Chem., Int. Ed.* **2021**, *60*, 21494.
[18] R. Schmuch, R. Wagner, G. Hörpel, T. Placke, M. Winter, *Nat. Energy* **2018**, *3*, 267.
[19] Y.-G. Lee, S. Fujiki, C. Jung, N. Suzuki, N. Yashiro, R. Omoda, D.-S. Ko, T. Shiratsuchi, T. Sugimoto, S. Ryu, J. H. Ku, T. Watanabe, Y. Park, Y. Aihara, D. Im, I. T. Han, *Nat. Energy* **2020**, *5*, 299.
[20] A. Kato, M. Yamamoto, A. Sakuda, A. Hayashi, M. Tatsumisago, *ACS Appl. Energy Mater.* **2018**, *1*, 1002.
[21] M. Yamamoto, Y. Terauchi, A. Sakuda, M. Takahashi, *J. Power Sources* **2018**, *402*, 506.
[22] D. H. Kim, H. A. Lee, Y. B. Song, J. W. Park, S.-M. Lee, Y. S. Jung, *J. Power Sources* **2019**, *426*, 143.
[23] B. A. Boukamp, G. C. Lesh, R. A. Huggins, *J. Electrochem. Soc.* **1981**, *128*, 725.
[24] L. Y. Beaulieu, K. W. Eberman, R. L. Turner, L. J. Krause, J. R. Dahn, *Electrochem. Solid-State Lett.* **2001**, *4*, A137.
[25] Y. Sun, N. Liu, Y. Cui, *Nat. Energy* **2016**, *1*, 16071.
[26] H. Wang, J. Fu, C. Wang, J. Wang, A. Yang, C. Li, Q. Sun, Y. Cui, H. Li, *Energy Environ. Sci.* **2020**, *13*, 848.
[27] M. Ge, C. Cao, G. M. Biesold, C. D. Sewell, S.-M. Hao, J. Huang, W. Zhang, Y. Lai, Z. Lin, *Adv. Mater.* **2021**, *33*, 2004577.
[28] M. B. Pinson, M. Z. Bazant, *J. Electrochem. Soc.* **2013**, *160*, A243.
[29] Y. S. Jung, K. T. Lee, S. M. Oh, *Electrochim. Acta* **2007**, *52*, 7061.
[30] M. Nie, D. P. Abraham, Y. Chen, A. Bose, B. L. Lucht, *J. Phys. Chem. C* **2013**, *117*, 13403.
[31] H. Sohn, D. H. Kim, R. Yi, D. Tang, S.-E. Lee, Y. S. Jung, D. Wang, *J. Power Sources* **2016**, *334*, 128.
[32] X. Wu, J. Billaud, I. Jerjen, F. Marone, Y. Ishihara, M. Adachi, Y. Adachi, C. Villevieille, Y. Kato, *Adv. Energy Mater.* **2019**, *9*, 1901547.
[33] E. Pollak, G. Salitra, V. Baranchugov, D. Aurbach, *J. Phys. Chem. C* **2007**, *111*, 11437.

[34] M. T. Mcdowell, S. W. Lee, W. D. Nix, Y. Cui, *Adv. Mater.* **2013**, *25*, 4966.
[35] A. Magasinski, P. Dixon, B. Hertzberg, A. Kvit, J. Ayala, G. Yushin, *Nat. Mater.* **2010**, *9*, 353.
[36] N. Liu, Z. Lu, J. Zhao, M. T. Mcdowell, H.-W. Lee, W. Zhao, Y. Cui, *Nat. Nanotechnol.* **2014**, *9*, 187.
[37] M. Ko, S. Chae, J. Ma, N. Kim, H.-W. Lee, Y. Cui, J. Cho, *Nat. Energy* **2016**, *1*, 16113.
[38] J. Kim, C. Kim, I. Jang, J. Park, J. Kim, U. Paik, T. Song, *J. Power Sources* **2021**, *510*, 230425.
[39] D. Cao, X. Sun, Y. Li, A. Anderson, W. Lu, H. Zhu, *Adv. Mater.* **2022**, *34*, 2200401.
[40] J. Y. Kim, S. Jung, S. H. Kang, J. Park, M. J. Lee, D. Jin, D. O. Shin, Y.-G. Lee, Y. M. Lee, *Adv. Energy Mater.* **2022**, *12*, 2103108.
[41] S. Cangaz, F. Hippauf, F. S. Reuter, S. Doerfler, T. Abendroth, H. Althues, S. Kaskel, *Adv. Energy Mater.* **2020**, *10*, 2001320.
[42] H. S. Tan Darren, Y.-T. Chen, H. Yang, W. Bao, B. Sreenarayanan, J.-M. Doux, W. Li, B. Lu, S.-Y. Ham, B. Sayahpour, J. Scharf, A. Wu Erik, G. Deysher, E. H. Hyea, J. Hah Hoe, H. Jeong, B. Lee Jeong, Z. Chen, S. Meng Ying, *Science* **2021**, *373*, 1494.
[43] I. Na, H. Kim, S. Kunze, C. Nam, S. Jo, H. Choi, S. Oh, E. Choi, Y. B. Song, Y. S. Jung, Y. S. Lee, J. Lim, *ACS Energy Lett.* **2023**, *8*, 1936.
[44] D. Cao, T. Ji, A. Singh, S. Bak, Y. Du, X. Xiao, H. Xu, J. Zhu, H. Zhu, *Adv. Energy Mater.* **2023**, *13*, 2203969.
[45] Y. Huang, B. Shao, Y. Wang, F. Han, *Energy Environ. Sci.* **2023**, *16*, 1569.
[46] M. J. Wang, E. Kazyak, N. P. Dasgupta, J. Sakamoto, *Joule* **2021**, *5*, 1371.
[47] T. Y. Kwon, K. T. Kim, D. Y. Oh, Y. B. Song, S. Jun, Y. S. Jung, *Energy Storage Mater.* **2022**, *49*, 219.
[48] J. Woo, Y. B. Song, H. Kwak, S. Jun, B. Y. Jang, J. Park, K. T. Kim, C. Park, C. Lee, K.-H. Park, H.-W. Lee, Y. S. Jung, *Adv. Energy Mater.* **2023**, *13*, 2203292.
[49] F. P. Mcgrogan, T. Swamy, S. R. Bishop, E. Eggleton, L. Porz, X. Chen, Y.-M. Chiang, K. J. Van Vliet, *Adv. Energy Mater.* **2017**, *7*, 1602011.
[50] S. Y. Han, C. Lee, J. A. Lewis, D. Yeh, Y. Liu, H.-W. Lee, M. T. Mcdowell, *Joule* **2021**, *5*, 2450.
[51] G. Lee, Y. Choi, H. Ji, J. Y. Kim, J. P. Kim, J. Kang, O. Kwon, D. W. Kim, J. H. Park, *Carbon* **2023**, *202*, 12.
[52] J.-S. Kim, G. Yoon, S. Kim, S. Sugata, N. Yashiro, S. Suzuki, M.-J. Lee, R. Kim, M. Badding, Z. Song, J. Chang, D. Im, *Nat. Commun.* **2023**, *14*, 782.
[53] B. Hertzberg, J. Benson, G. Yushin, *Electrochem. Commun.* **2011**, *13*, 818.
[54] P. K. Parashar, V. K. Komarala, *Sci. Rep.* **2017**, *7*, 12520.
[55] H. Lim, S. Jun, Y. B. Song, H. Bae, J. H. Kim, Y. S. Jung, *Energy Storage Mater.* **2022**, *50*, 543.
[56] N. Liu, L. Hu, M. T. Mcdowell, A. Jackson, Y. Cui, *ACS Nano* **2011**, *5*, 6487.
[57] R. Zhan, X. Wang, Z. Chen, Z. W. Seh, L. Wang, Y. Sun, *Adv. Energy Mater.* **2021**, *11*, 2101565.
[58] E. Adhitama, F. Dias Brandao, I. Dienwiebel, M. M. Bela, A. Javed, L. Haneke, M. C. Stan, M. Winter, A. Gomez-Martin, T. Placke, *Adv. Funct. Mater.* **2022**, *32*, 2201455.
[59] K. H. Kim, J. Shon, H. Jeong, H. Park, S.-J. Lim, J. S. Heo, *J. Power Sources* **2020**, *459*, 228066.
[60] X. Liang, Q. Pang, I. R. Kochetkov, M. S. Sempere, H. Huang, X. Sun, L. F. Nazar, *Nat. Energy* **2017**, *2*, 17119.
[61] N. Ohta, K. Takada, I. Sakaguchi, L. Zhang, R. Ma, K. Fukuda, M. Osada, T. Sasaki, *Electrochem. Commun.* **2007**, *9*, 1486.
[62] Y. J. Nam, D. Y. Oh, S. H. Jung, Y. S. Jung, *J. Power Sources* **2018**, *375*, 93.
[63] S. Jun, Y. J. Nam, H. Kwak, K. T. Kim, D. Y. Oh, Y. S. Jung, *Adv. Funct. Mater.* **2020**, *30*, 2002535.
[64] R.-M. Gao, H. Yang, C.-Y. Wang, H. Ye, F.-F. Cao, Z.-P. Guo, *Angew. Chem., Int. Ed.* **2021**, *60*, 25508.
[65] Y.-N. Li, C.-Y. Wang, R.-M. Gao, F.-F. Cao, H. Ye, *Energy Storage Mater.* **2021**, *38*, 262.
[66] S. Wenzel, S. J. Sedlmaier, C. Dietrich, W. G. Zeier, J. Janek, *Solid State Ionics* **2018**, *318*, 102.